Journal of Materials Research and Technology 27 (2023) 8244–8257

Contents lists available at ScienceDirect

Journal of Materials Research and Technology

journal homepage: www.elsevier.com/locate/jmrt

Influence of deformation path on the stress state and damage evolution along the central axis of a large size forged ingot of AISI H13 steel

Prashant Dhondapure [a], Pierre Tize Mha [a], Soumyaranjan Nayak [b], Lea Ebacher [a], Simin Dourandish [a], Henri Champliaud [a], Jean-Benoit Morin [c], Mohammad Jahazi [a,*]

[a] Department of Mechanical Engineering, École de Technologie Supérieure, 1100 Notre Dame West, Montreal, Quebec, H3C 1K3, Canada
[b] Department of Metallurgical Engineering and Materials Science, Indian Institute of Technology Bombay, Mumbai, 400076, India
[c] Finkl Steel-Sorel Inc., 100 McCarthy, Saint-Joseph-de-Sorel, Quebec, J3R 3M8, Canada

ARTICLE INFO

Handling editor:L Murr

Keywords:
Cogging
Center burst formation
AISI H13
die geometry
FE analysis
Damage evolution

ABSTRACT

Development of cracks along the center axis of large high strength steel bars commonly occurs during the forging and leads to excessive part rejections. The present investigation aims to develop a better understanding of the evolution of stress-strain states during the forging operation and in particular the effect of deformation path illustrated by die geometry, on the evolution of damage during the cogging of an AISI H13 steel. Hot compression and tensile tests were performed using Gleeble-3800 thermo-mechanical simulator to develop the optimum material model which was then implemented in the finite element (FE) code Forge NxT 3.2® using a developed user subroutine. Normalized Cockcroft and Latham damage criterion and maximum shear stress (Tresca's) theory of failure were used to predict the damage and failure in the center axis of the shaft through FE analysis with three different die shapes: concave, flat, and convex. A comparative study between the three die geometries was conducted to quantify the effects of each of them on the sensitivity to central burst damage. FE model was validated using industrial data. The lowest and highest damage values were found to occur in the case of cogging with concave and flat die, respectively. The coefficient of variation (CoV) is employed as a measure of heterogeneity and it was found that the concave die provides more uniform deformation and most favorable results for the cogging compared to the flat and convex dies. The novel approach, application of concave die successfully implemented at the industrial scale cogging.

1. Introduction

Cogging is a forging process to manufacture different types of straight and stepped shafts from rectangular or square blocks by application of compressive force. Large industrial size forged shafts made of AISI H13 tool steels are widely used in the energy and transportation industries [1,2]. The manufacturing of large ingots especially high strength steels consists of melting in an electric arc furnace, followed by degassing, ingot casting, open die forging, and finally quench and temper operations before machining. Open die forging of large size ingots consists of upsetting, Free from Mannesmann effect (FM), and cogging process [3]. The formation and propagation of a defect, known as center burst, along the center axis during hot deformation (rolling, forging, etc.) of high strength steels is often observed in the industry and reported in the literature [4]. The occurrence of this defect brings unrecoverable damage to the part and results in total or partial rejection [5,6]. Therefore, to address the issue it is very important to identify and quantify the role of each of the manufacturing process parameters that lead to center burst defect formation.

AISI H13 is a high strength highly alloyed steel characterized by high molybdenum and vanadium contents that significantly increase the resistance to hot deformation [7,8]. Therefore, forging of AISI H13 alloy is challenging due to the high sensitiveness to high temperature deformation and high resistance to deformation at lower forging temperatures. Han et al. [9] reported that the application of higher forging loads is not a viable solution as it could lead to even more center burst defects during the cogging process. Fig. 1(a) shows the center burst formation at extreme end of the workpiece indicated with an arrow. Fig. 1(b) shows the propagation of the center burst defect along the center axis of the workpiece found during the quality check. Yang et al. [10] it have been reported that the center burst defect will propagate through the central axis of a workpiece (as shown in Fig. 1) with increase in number of

* Corresponding author.
E-mail address: mohammad.jahazi@etsmtl.ca (M. Jahazi).

https://doi.org/10.1016/j.jmrt.2023.11.206
Received 12 October 2023; Received in revised form 21 November 2023; Accepted 22 November 2023
Available online 28 November 2023

passes under the radial compression.

In the literature, the available data on the formation of center crack and burst is mostly related to Cross Wedge Rolling (CWR) process, and very little or no data is reported on cogging. Although, fundamentally cogging and CWR are similar as radial compression is the most important loading in both cases. Hence, an analysis of the published literature on center burst cracking during the CWR process is provided hereafter. Lee et al. [11] found that center cracks formed during the CWR process in the middle of the shaft in both radial and axial directions.

Zhou et al. [12–14] studied the central crack formation during the cross wedge rolling of pure aluminum using FE analysis and lab scale experiments and proposed damage criteria to predict the risk of center crack formation. They reported that the maximum tensile and shear stresses were the key parameters for damage occurrence along the center axis of the workpiece. Li et al. [15] studied experimentally the center crack formation in a 1100H16 aluminum alloy and investigated the mechanisms responsible for ductile fracture at the center of the workpiece. They reported that significant void formation and propagation occurred along the center axis of the workpiece, induced by shear and tensile stresses, respectively. Kukuryk [16] used normalized Cockcroft and Latham damage criteria for the prediction of damage during multi pass cogging of lab scale specimens made of 30CrMoV1211 steel and reported that tensile stresses were the primary factor influencing the initiation of discontinuities along the center axis of the workpiece. In a recent study, the same authors Kukuryk et al. [17] studied a two-stage cogging process of a X5CrNi18-10 stainless steel, using flat and shaped anvils, and calculated the distribution of effective strain and stress, mean stress, and stress triaxiality in the radial direction. They identified the damage criteria that best represented the center burst cracking during the cogging of the investigated alloy.

Very little data is available in the open literature on the formation of center burst during the cogging of high strength steel bars and even less in relation to AISI H13 steel, despite the important industrial applications of this steel [18–20]. The reported studies have focused on relating material tearing and center burst formation to the evolution of the flow curve on laboratory scale compression samples and not assessing the risk of center burst formation as a function of deformation conditions representing the cogging process. The data is even more scarce when it comes to the influence of *die geometry* on stress-strain states and damage evolution at the center of the workpiece during the cogging process of large size round bars [21,22]. Most of the existing data on the influence of die geometry is on void closure. Kukuryk et al. [16] studied the effect of flat, v-shaped die and assembly of three radial dies on void closure on a X40CrMoV511 steel. The authors found that v-shaped die was the most efficient in closing axial voids of various sizes, as compared to the other types of dies. Dudra et al. [23] analyzed the influence of flat, v-shape, and Mannesmann effect-free dies on void closure during open die forging. This analysis was based on effective strain and hydrostatic stresses at the center of the billet. The authors reported that effective strain was a better indicator for void closure. Zhang et al. [24] studied the effect of die geometry on void closure during the forging of a heavy ingot using multi scale FE analysis. They reported that cymbal shape and v-shape die provided the best results for voids closing around the axis and near to the die surface during upsetting and cogging operations, respectively. Tamura et al. [25] employing rigid plastic finite element analysis for open die forging, optimized die curvature radius to ensure void closure in a stainless steel bar using the criterion based on equivalent plastic strain value. Kukuryk [26] studied the effect of convex die, assembly of three radial anvils and skew anvils die surface on stress-strain states during the cogging of a X32CrMoV12-28 die steel. The authors concluded that by variation of die curvature, stress-strain states can be varied in the absence of tensile stresses along the center axis of the workpiece and proposed a criterion to predict the damage. Ghiotti et al. [27] reported the formation of the Mannesmann defect during rolling, cogging, and cross wedge rolling along the longitudinal axis of a steel bar. They proposed a model to predict the Mannesmann effect at the center of the bar using a damage law that considered the impact of flaws already present in the metal during the fabrication process. Recently, Lin et al. [28] studied the effect of flexible rollers on the defects present at the center of a C45 steel bar during skew rolling. The authors determined deformation conditions that would minimize the tensile and shear stresses in order to avoid the formation of central defects along the center axis of the workpiece. Successfully produced rolled bar free from the center defect in absence of Mannesmann effect.

Based on the above literature review it can be said that the crucial factors affecting the occurrence of center cracks and bursts during radial compression include maximum tensile stress, maximum shear stress, and stress-strain states at the center of the workpiece. This study aims to identify the key deformation parameters that increase the sensitivity to center burst defect formation and propagation during the cogging process of an AISI H13 steel and in particular determine the effect of die geometry on stress-strain states and the center burst damage evolution. A secondary objective is then to develop a predictive model and apply it to an industrial size workpiece. To this end, the optimum constitutive model, which provided the most accurate flow stress prediction, was determined and integrated into the Forge NxT 3.2® FEM code using a specially developed subroutine. The FE simulation of cogging process using concave, flat and convex die were performed. The critical damage value in the range of examined forging temperatures was calculated for the AISI H13 steel and used for the prediction of risky zones for burst formation. The validated FE model is used for the prediction of center burst formation during the cogging of AISI H13 steel on an industrial scale.

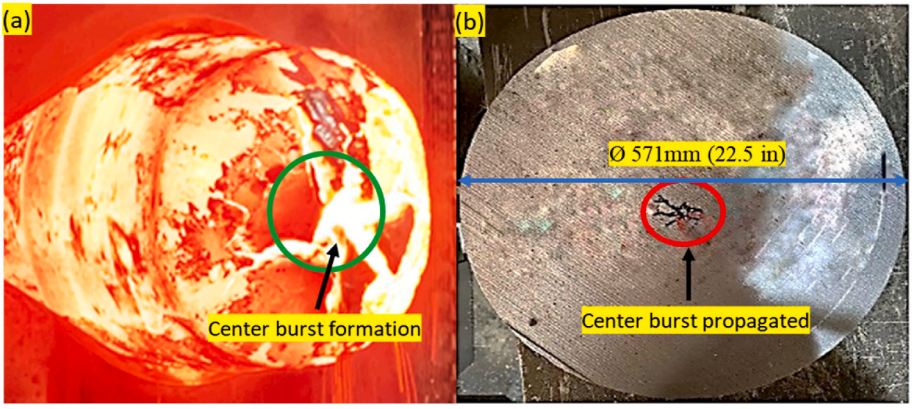

Fig. 1. Center burst occurred during the cogging of AISI H13 steel (a) center burst formation at extreme end of the workpiece (b) center burst propagated along the center axis of the workpiece.

2. Material and experimental procedure

2.1. Material

The material used in this study was manufactured and provided by Finkl Steel-Sorel, Quebec, Canada. The production process commenced with the melting of scrap metal through an electric arc furnace, followed by refining and degassing to control the alloy composition. The melting process was followed by ingot casting and solidification. The solidified ingot was transferred to the forging furnace and heated up to 1260 °C before the forging and post forging heat treatment processes. Tensile and compression test specimens were machined from the quarter location of the 571 mm diameter shaft. Table 1 shows the chemical composition of the AISI H13 steel in weight percentage.

2.2. Experimental procedure

2.2.1. Hot compression test

Hot compression tests were conducted using Gleeble-3800® thermo-mechanical simulator to obtain flow curves for AISI H13 steel and develop the material model for the finite element analysis of the cogging process. The samples with a diameter of 10 mm and a height of 15 mm were produced in accordance with the ASTM E209 standard. A preliminary analysis of the industrial conditions (press charts, temperature measurements, die velocity, etc.) allowed for the determination of deformation temperatures, reduction per pass, strain rates, and strain. Fig. 2 illustrates the laboratory test conditions, encompassing three temperatures 1260 °C, 1200 °C, and 1150 °C, coupled with four strain rates 0.001 s^{-1}, 0.01 s^{-1}, 0.1 s^{-1}, and 1 s^{-1} that are representative of the industrial forging process. The specimen was heated up to a temperature of 1260 °C at a heating rate of 2 °C/s and maintained for 15 min to guarantee consistent temperature across the entire volume. It was then cooled at a rate of 1 °C/s to the test temperature. After reaching the test temperature, it was held for 1 minute before deformation was applied. Nickel based paste and 0.1 mm tantalum sheet were placed between the anvil and the specimen's surface to minimize the friction during deformation. The sampling rate was adjusted to ensure an equal number of data points were recorded at all strain rates. After the hot compression test, the flow stress data was automatically exported from the Gleeble 3800 in OriginLab® software on the computer connected to the controller. Fig. 3 presents the measured true stress-strain curve subsequent to the hot compression test, considering all possible combinations of process parameters (3 temperatures and 4 strain rates). Flow curves in Fig. 3, demonstrate both the occurrence of hardening and softening phenomena at lower strain rates of 0.001 s^{-1} and 0.01 s^{-1}, while only hardening is noticeable at strain rates of 0.1 s^{-1} and 1 s^{-1}.

2.2.2. Hot tensile test

The main objective out of the hot tensile testing was to calculate the critical damage value in the range of forging temperature and deformation rate for AISI H13 using normalized Cockcroft and Latham criterion. The hot tensile test specimens (gauge length = 66 mm and diameter = 6.25 mm) were prepared according to ASTM E8 standard [29]. Fig. 4(a) shows the tensile setup inside the Gleeble 3800 thermo-mechanical simulator chamber with an installed extensometer to measure the elongation in the gauge length of the specimen. Fig. 4(b) shows the tensile specimen before and after the test with dimensions. Fig. 5(a) shows the heating and tensile testing sequence at two distinct temperatures, 800 °C and 1200 °C, employing a strain rate of 0.05 s^{-1}. Test specimen diameter and length, both before and after the test, were recorded to calculate the percentage reduction in cross-sectional area and the elongation. Like the compression test data, tensile test data were also recorded and automatically exported in OriginLab® software. Fig. 5 (b) shows the true stress-strain curves after the hot tensile test.

Table 1
Composition of chemical elements in AISI H13 steel.

Elements	C	Mn	Si	Cr	Mo	V	Fe
Weight %	0.4	0.4	1.05	5.15	1.35	1	Balance

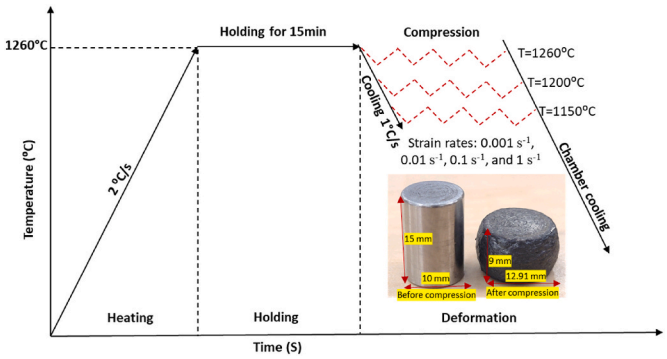

Fig. 2. Heating and thermomechanical testing cycle.

3. Identification of constitutive law parameters and calculation of damage value

3.1. Arrhenius model

The established model [30] provides the relation between critical factors for hot deformation, such as strain rate, temperature and activation energy, while maintaining a constant deformation value. The relationship is presented in Eq. (1) where Z is known as the Zener-Hollomon parameter:

$$Z = \dot{\varepsilon}\, e^{\left(\frac{Q}{RT}\right)} \tag{1}$$

In the above equation, Q represents the activation energy (kJ.mol^{-1}), R stands for the universal gas constant (kJ.mol^{-1}.K^{-1}) and A, α and n are constants specific to the material.

Arrhenius model also provides the relation between strain rate, flow stress, and deformation temperature, given by Eq (2).

$$\dot{\varepsilon} = \mathrm{AF}(\sigma) e^{\left(-\frac{Q}{RT}\right)} \tag{2}$$

Here, F(σ) takes the form of a power function, exponential function, or Hyperbolic sine function as presented below:

$$F(\sigma) = \sigma^{n_1} \ (\alpha\sigma < 0.8) \tag{3}$$

$$F(\sigma) = e^{(\beta\sigma)} \ (\alpha\sigma > 1.2) \tag{4}$$

$$F(\sigma) = [\sinh(\alpha\sigma)]^n \ (For\ all\ \sigma) \tag{5}$$

$$\alpha = \frac{\beta}{n_1} \tag{6}$$

In this context, A, n, n_1, β and α represent material constants, with the additional relationship in Eq. (6). Combining the equations above, provides the expression for the flow stress, which primarily depends on the values of α, Z, A and n. The corresponding values for these material constants were determined through regression analysis and the results are reported in Table 2 for a strain of 0.5.

On the basis of the above equations, the flow stress could be expressed as:

$$\sigma = \frac{1}{\alpha} ln \left\{ \left(\frac{Z}{A}\right)^{\frac{1}{n}} + \left[\left(\frac{Z}{A}\right)^{\frac{2}{n}} + 1 \right]^{1/2} \right\} \tag{7}$$

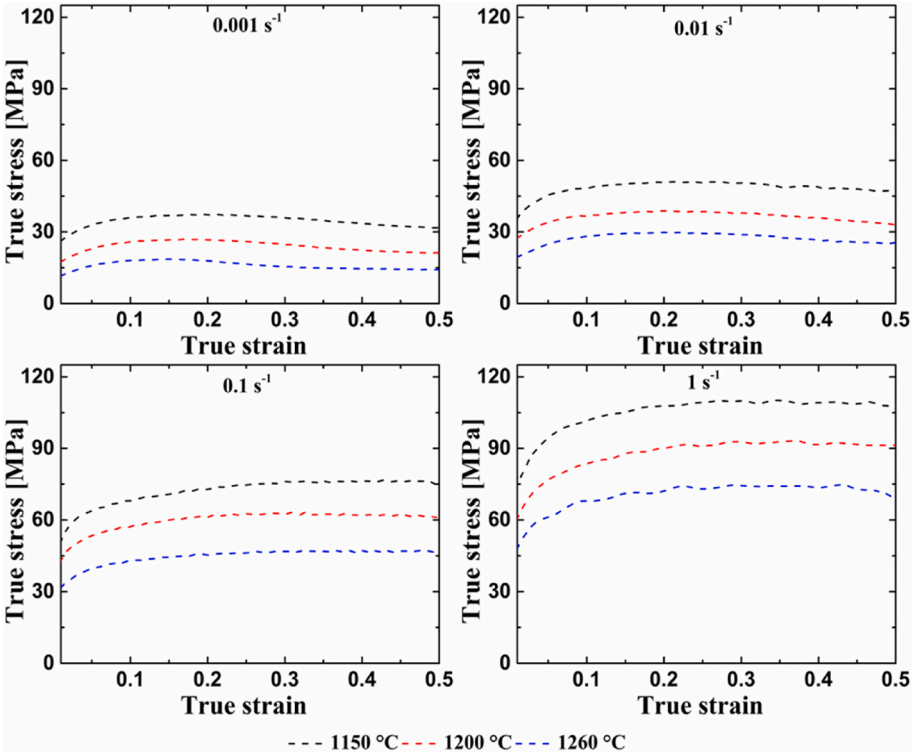

Fig. 3. Flow stress behavior of AISI H13 steel after the hot isothermal compression.

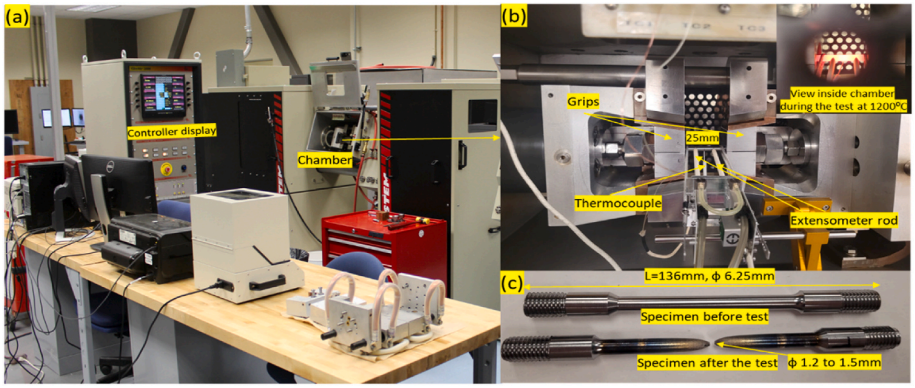

Fig. 4. Experimental setup (a) Gleeble 3800 thermo-mechanical simulator (b) tensile test setup inside the Gleeble chamber (c) tensile specimen before and after the test.

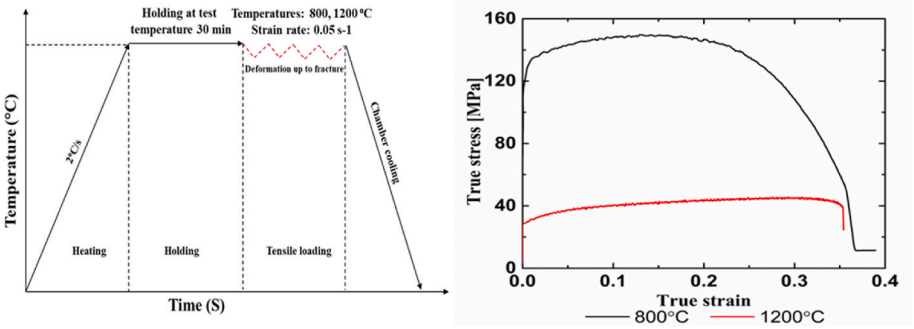

Fig. 5. (a) The heating and deformation process (b) true stress-strain plot for AISI H13 steel following a hot tensile test at strain rate 0.05 s^{-1}.

Table 2
Material parameters for the Arrhenius Model at strain 0.5

$\beta(MPa^{-1})$	n_1	$\alpha(MPa^{-1})$	n	$Q(K\ J\ mol^{-1})$	$lnA\ (s^{-1})$
0.1230	5.9313	0.0207	4.36	503.079	16.067

The material constants mentioned above in Table 2 were determined for a fixed value of strain (0.5). As shown in Fig. 3, when the strain increases from 0.01 to 0.5, the flow stress exhibits both hardening and softening behaviors in the material and therefore, it must be considered in the analysis [31,32]. To address the impact of strain on flow stress, a modified Arrhenius model, known as the strain-compensated model [33], was used in the present study. The material parameters α, n, Q, and A were formulated as functions of strain by employing polynomial functions of degree six. These functions are detailed and provided in expressions (8-11). Table 3 provides the material parameters for the strain-compensated model, along with the coefficients of the polynomial function.

$$\alpha = B_0 + B_1\varepsilon + B_2\varepsilon^2 + \cdots\cdots\cdots + B_m\varepsilon^m \tag{8}$$

$$n = C_0 + C_1\varepsilon + C_2\varepsilon^2 + \cdots\cdots\cdots + C_m\varepsilon^m \tag{9}$$

$$Q = D_0 + D_1\varepsilon + D_2\varepsilon^2 + \cdots\cdots\cdots + D_m\varepsilon^m \tag{10}$$

$$lnA = E_0 + E_1\varepsilon + E_2\varepsilon^2 + \cdots\cdots\cdots + E_m\varepsilon^m \tag{11}$$

3.1.1. Hansel-Spittel and Johnson-Cook models

The Hansel-Spittel [34] and Johnson-Cook models [35] are phenomenological material models widely used for the prediction of material response during high temperature deformation. Both models have been implemented as default in many materials FE modeling software [36]. They take into consideration temperature and strain rate dependencies and consider the occurrence of both hardening and softening phenomena during the material's hot deformation process [37]. Eq. (12), depicts the mathematical formulation of the Hansel-Spittel model, establishing the relationship between flow stress and the material parameters.

$$\sigma = A_o e^{m_1 T}\varepsilon^{m_2}\dot{\varepsilon}^{m_3} e^{\frac{m_4}{\varepsilon}}(1+\varepsilon)^{m_5 T} e^{m_6\varepsilon}\dot{\varepsilon}^{m_7 T^{m_8}} \tag{12}$$

Where, σ represents stress (MPa), $\dot{\varepsilon}$ stands for strain rate (s^{-1}), ε indicates strain, T represents the deformation temperature (°C) and A, m_1 through m_8 are specific material constants reported in Table 4.

Fig. 6 shows a comparison of flow stresses between experimental and Arrhenius model predicted values. Dashed lines represent the experimental data, while solid lines represent the predicted values. The difference between the measured and predicted values is small. However, this difference becomes more pronounced as the strain rate increases and temperature decreases. In Fig. 7 a comparison of flow stress between experimental and Hansel-Spittel model predicted values is presented. The difference between measured and predicted values are clearly higher compared to the Arrhenius model, especially at higher strain rates $0.1s^{-1}$ and $1s^{-1}$. Notably, for the lowest temperature of 1150 °C and highest strain rates, the Hansel-Spittel model is unable to predict the softening behavior of the AISI H13 material. The quantification of error and R-square values for the predicted flow stresses by the Arrhenius and Hansel-Spittel models is addressed in the subsequent section.

Table 3
Coefficient of polynomial function for modified Arrhenius model for the AISI H13.

α	n	$Q(\times 10^{-6})$	lnA
B_0 = 0.0324	C_0 = 4.435	D_0 = 0.556	E_0 = 40.9638
B_1 = -0.294	C_1 = -7.379	D_1 = -0.353	E_1 = -23.1777
B_2 = 2.9275	C_2 = 144.102	D_2 = -4.033	E_2 = -391.262
B_3 = -15.482	C_3 = -1106.84	D_3 = 42.129	E_3 = 3803.6
B_4 = 44.606	C_4 = 3735.17	D_4 = -144.929	E_4 = -12996.1
B_5 = -65.421	C_5 = -5896.13	D_5 = 206.846	E_5 = 18786.2
B_6 = 38.146	C_6 = 3577.77	D_6 = -101.488	E_6 = -9517.32

Fig. 8(a) and **8(b)** provide a comparison between experimental and predicted flow stress values using both constitutive models. The evaluations were conducted using the average absolute relative error (AARE) and R-square values. AARE values, computed using Eq. (13), were employed to assess the efficiency of flow stress prediction by the two models. AARE values for Arrhenius and Hansel- Spittel model were found to be 3.6 % and 5.7 %, respectively. R-square values were calculated for Arrhenius and Hansel-Spittel model were found to be 0.9936 and 0.9802, respectively. A similar analysis, which will not be detailed here, was conducted for the Johnson-Cook model and led to similar results. Specifically, for the same data set, AARE and R-square values were found to be 13.5 % and 0.89, respectively. Finally, it must be noted that comparable findings for both models were reported by Ref. [38]. for modified-H13 steel.

$$AARE = \frac{1}{N}\sum_1^N \left|\frac{\sigma_e^i - \sigma_p^i}{\sigma_e^i}\right| \times 100 \tag{13}$$

Where, σ_e represents the experimental flow stress value, and σ_p denotes the predicted flow stress value.

The above analysis showed that predictions from the Arrhenius model demonstrated higher accuracy and closer alignment with the experimental flow stress values compared to Hansel-Spittel and Johnson and Cook models. As a result, the Arrhenius model was integrated into Forge NxT 3.2® software to simulate the cogging process and predict the stress, strain, and damage evolution map at the end of cogging.

3.2. Normalized Cockcroft and Latham criterion

This criterion relies on the evolution of the maximum tensile principal stress, effective stress-strain, and strain at the point of fracture. Oh and Kobayashi [39] proposed a ductile damage criterion to identify the regions prone to ductile damage and crack initiation. During the forging process, ductile failure occurs due to the accumulation of plastic tensile strain and tensile stresses. The damage value reflects the accumulation of damage during the metal forming process [40,41]. The critical damage value varies with temperature and strain rate. Stefanik et al. [42] examined the impact of these parameters on a BSt500S steel and observed that as temperature and strain rate rise, the limiting damage value also increases. Eq. (14) and Eq. (15) provide the relationship between the critical damage value and material properties at a given temperature and strain rate. Both equations are available in the Forge NxT 3.2® [43]. In the present work, the damage values were calculated based on the percentage reduction in cross-section area using Eq. (15) at a constant temperature and strain rate. Table 5 provides the hot tensile properties as well as the damage values at 800 °C and 1200 °C, for a strain rate of 0.05 s^{-1} determined from the hot tensile tests. Interpretation of cogging results were based on the yield strength and damage values to predict the risky zones for the center burst defect formation and propagation.

$$C_{CR} = \int_0^{\bar{\varepsilon}_f}\left(\frac{\sigma_1}{\bar{\sigma}}\right)d\bar{\varepsilon} \tag{14}$$

$$C_{CR} \approx 1.5 \times \mathrm{In}\left(1 + \frac{A\%}{100}\right) \tag{15}$$

Where, $\bar{\varepsilon}$ is the equivalent strain, $\bar{\varepsilon}_f$ is the strain at fracture, σ_1 is the maximum principal stress, $\bar{\sigma}$ is the effective stress, A% is the reduction of cross section near to fracture.

Table 4
Material parameters for Hansel - Spittel model.

A	m_1	m_2	m_3	m_4	m_5	m_6	m_7	m_8
3×10^{11}	−0.0027	0.2380	0.1888	−0.0001	−0.0010	−0.0457	−2.5382	0

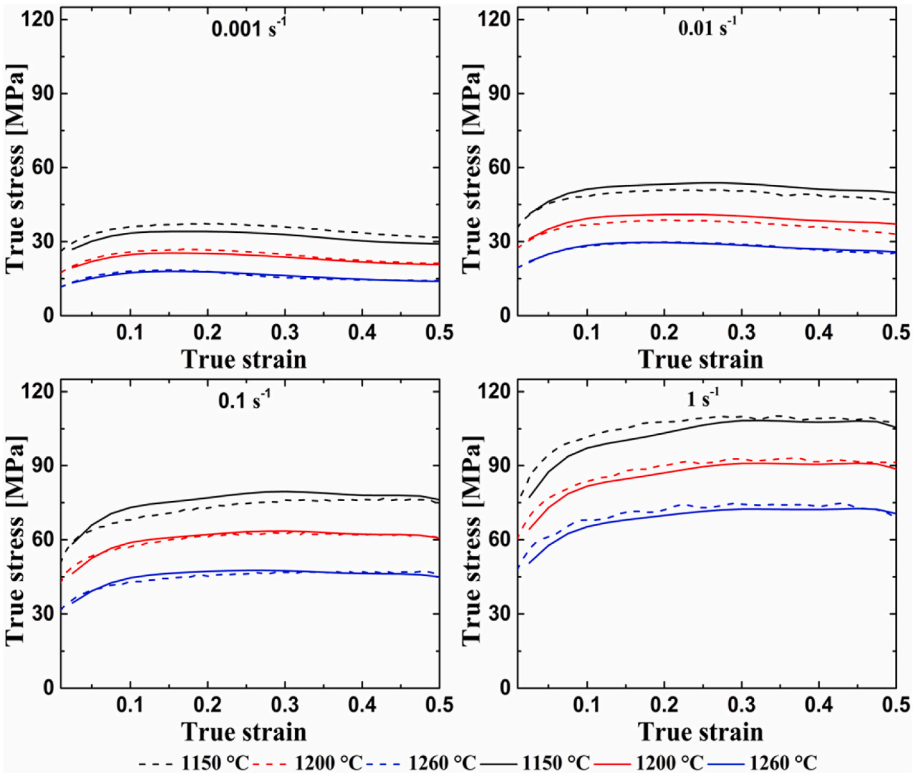

Fig. 6. Contrasting between experimental (dashed) and predicted (solid) flow stress using the Arrhenius model.

4. Finite element modeling and analysis

The industrial cogging process was simulated using commercial finite element software Forge NxT 3.2®. A three-dimensional finite element model was employed for this analysis. Fig. 9 shows the finite element model along with the mesh geometry that was used for simulating the cogging process. The three die geometries concave, flat and convex, that were used for the simulation are shown in Fig. 9(a–c). The discretized FE model was used for the numerical simulation with four node tetrahedron elements and mesh sensitivity analysis was performed to ensure the accuracy of output results. The boundary conditions used in the finite element analysis were similar to the industrial process. This encompassed factors such as the initial billet temperature, deformation rate, amount of deformation applied per blow, and the heat transfer aspects with the environment and the die-workpiece interface. Table 6 provides the details of the input boundary conditions used for the FE analysis.

The dimensions of the flat and curve dies were 304 mm × 406 mm x 1016 mm and the radius of curvature for the curve dies was 203 mm. During the cogging process, the initial billet with a square cross section of 711 mm × 711 mm x 2540 mm was positioned between the upper and lower dies along their edges. At end of every pass, the billet was rotated by 90, 45, and 22.5° to begin the next pass. This process is repeated until a target round shaft with a diameter of approximately 571 mm was obtained. Fig. 10 shows the finite element model at the end of the cogging process. Fig. 10(a-c) show equivalent strain distribution with concave, flat and convex dies, respectively. The results show that the flat die created higher equivalent strain values compared to the concave and convex dies curvature. It is interesting to note that to reach the same final dimensions concave, flat and convex dies required number of passes were 12, 19, and 16, respectively.

Moreover, it can be seen that for the same amount of deformation, concave die produces more deformation compared to flat and convex die. Therefore, the concave die requires a smaller number of passes to achieve the final dimensions of the shaft and complete the cogging process.

4.1. Industrial setup and validation of FE model

Fig. 11 shows the forging setup at the partner industry, Finkl steel, Sorel, Quebec, Canada. Fig. 11(a) shows the 2000 metric tons forging press. Fig. 11(b-c) shows concave and flat die setups for the cogging of AISI H13 steel, respectively. Press pressure and position data were collected during the cogging operation. Using press pressures, forging loads were calculated in metric tons and with press position data, strain rate and percent deformation were calculated. Fig. 12 shows the comparison of predicted and measured maximum force for each blow during cogging for the first two passes. It must be noted that, 8 blows were considered in each pass. Fig. 12(a-b) shows the comparison between predicted and measured maximum force versus number of blows for concave and flat dies, respectively. Specifically, it can be seen that as contact area between the die and the workpiece surface for the concave die is higher compared to the flat die; as a result, the concave die shows a higher value of maximum force. The average absolute relative error between measured and predicted maximum force were calculated for concave and flat dies, and were found to be ≈ 7 % and ≈5.3 %,

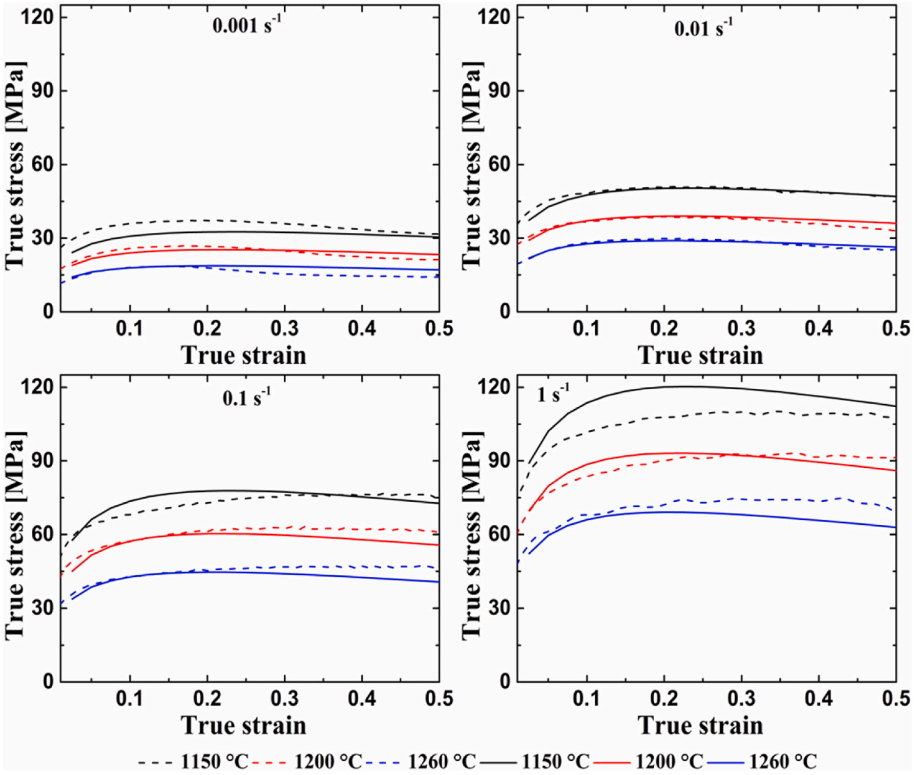

Fig. 7. Contrasting between experimental (dashed) and predicted (solid) flow stress using the Hansel-Spittel.

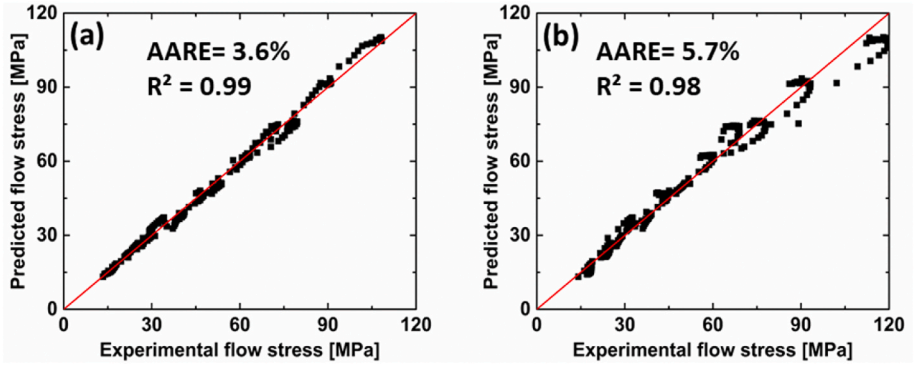

Fig. 8. Comparison of accuracy and correlation between experimentally measured and predicted flow stress values by employing (a) Arrhenius model and (b) Hansel - Spittel model.

Table 5
AISI H13 steel hot tensile properties and corresponding damage value.

Temperature (°C)	Yield strength (MPa)	Final diameter at necking c/s (mm)	% Reduction in cross section area	Critical damage value (C_{CR})
800	125	~1.5	94	0.99
1200	29	~1.2	96.5	1.01

respectively. Comparative analysis shows good agreement between predicted and measured maximum forces. Measured force gives slightly higher value compared to the predicted due to the differences in friction conditions. Fig. 1(b) and **13** show that final diameter of the shaft at end of cogging process in the industry and at end of FE analysis were very close to each other. AARE value was found to be less than 2 %; thereby, confirming the validity of the findings.

Fig. 13 shows the distribution map of equivalent strain along the longitudinal and transverse cross sections of the shaft at the end of the cogging process. The left and right transverse cross sections were captured at the extreme end and center of the shaft, respectively. The figures in the right cross section display the resulting diameter of the shaft after the simulation using the corresponding die geometries. Following the completion of the cogging process, there is a greater accumulation of equivalent strain at the center of the shaft on the cross section located at the extreme end, in contrast to the cross section at the center. The concave die exhibits a more uniform distribution of equivalent strain across all regions of the shaft, including the surface, center, and extreme edges, in comparison to the convex and flat dies. The outcomes indicate localized deformation along the center axis and extreme edges with the flat die. Conversely, the convex die induces localized deformation at the surface and just below the surface because of its sharper curvature, differing from the concave and flat dies.

Fig. 14 presents the distribution of damage values on both the longitudinal and transverse cross sections of the shaft upon completion of

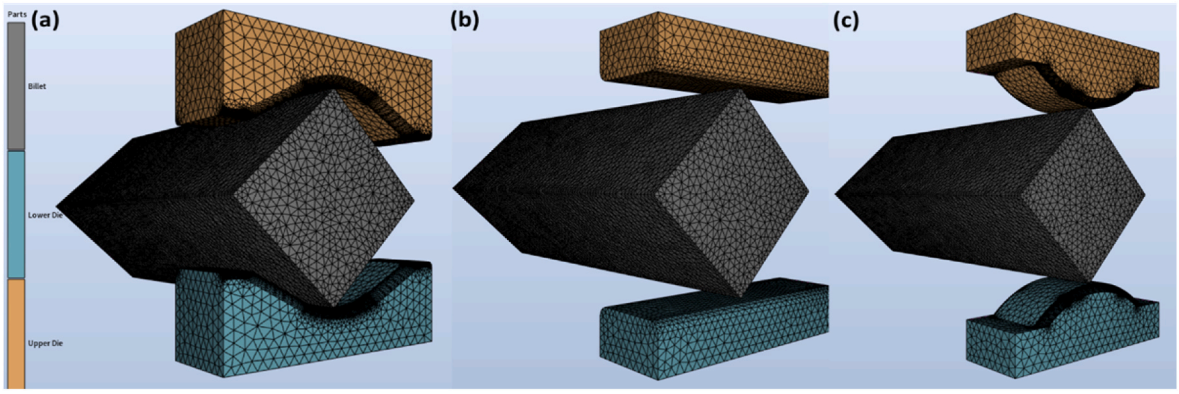

Fig. 9. Finite element model for cogging simulation before deformation with (a) concave (b) flat and (c) convex die.

Table 6
Input boundary conditions for FE analysis.

Parameters	Input to FE model
Square ingot and initial dimensions	711 mm × 711 mm x 2540 mm
Upper and lower die	Concave, flat and convex
Ingot initial temperature	1260 °C
Die temperature	35 °C
Die velocity	15 mm/s
Material	AISI H13 steel
Material model	Arrhenius
Displacement per blow	165 mm
Mesh size	26 mm (tetrahedron)
Number of mesh elements	126121 (workpiece)
Heat Transfer coefficient with air	10 W m^{-2} K^{-1}
Heat Transfer coefficient with die	10000 W m^{-2} K^{-1}
Friction condition	No lubrication
Manipulator	Assumed holds one end of the ingot

the cogging process. The pattern of damage value distribution aligns with that of the equivalent strain distribution. Left and right transverse cross sections were taken at the extreme end and at the center of the shaft, respectively. Upon completing the cogging process, it was observed that damage accumulation at the center of the shaft's extreme end cross section was more pronounced compared to the center cross section. This disparity can be attributed to varying stress-strain conditions. When employing the concave die, damage distribution exhibited uniformity across the surface, central region, and extreme edges of the shaft. In contrast, the flat and convex dies displayed non-uniform damage distribution. The most substantial damage was identified at the extremities and along the central axis of the shaft. These outcomes align closely with experimental observations, indicating that the shaft's extremities were more susceptible to damage, which in turn could initiate cracks and lead to burst formation. Yang et al. [10] reported that after burst formation with an increase in the number of passes, crack propagation took place along the longitudinal axis through the center of the shaft.

5. Results and discussion

5.1. Identification of the key parameters

To analyze the cogging process, data was collected at the end of each pass. For data recording, two distinct regions were selected: the two ends and the central area of the shaft. This selection was prompted by the non-uniform distribution of deformation and damage along the longitudinal axis. Fig. 15 shows the placement of sensors in simulation used for data acquisition. Sensors 1 to 5 were positioned along the longitudinal cross section, aligned with the center axis of the shaft. Sensors 1 and 5 were located at the two extreme ends, while sensors 2, 3, and 4 were positioned within the central regions of the shaft. Equivalent strain, damage value, maximum shear stress and stress triaxiality variations were plotted to show how the average values from the two extreme ends (1 and 5) compare to the average values from the central region (2, 3, and 4) in relation to the number of passes. This analysis is presented in the following.

5.1.1. Equivalent strain distribution

Fig. 16 depicts the change in the equivalent strain as the number of passes increases throughout the cogging process. The results show a linear increase with the increasing number of passes. Notably, the average equivalent strain value at the two ends surpassed the average value within the central region of the shaft at the end of each pass. The

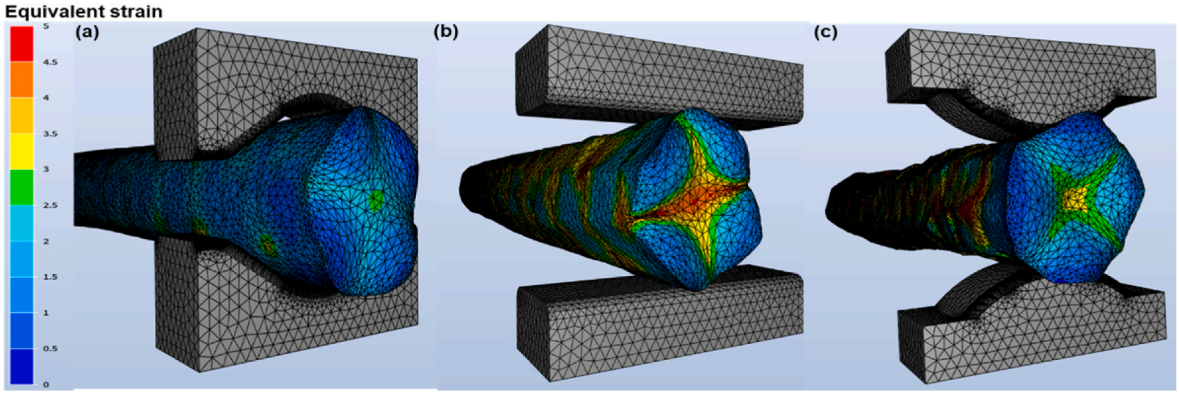

Fig. 10. Finite element model for cogging simulation after deformation at the end of cogging showing the effective strain distribution with (a) concave (b) flat and (c) convex die.

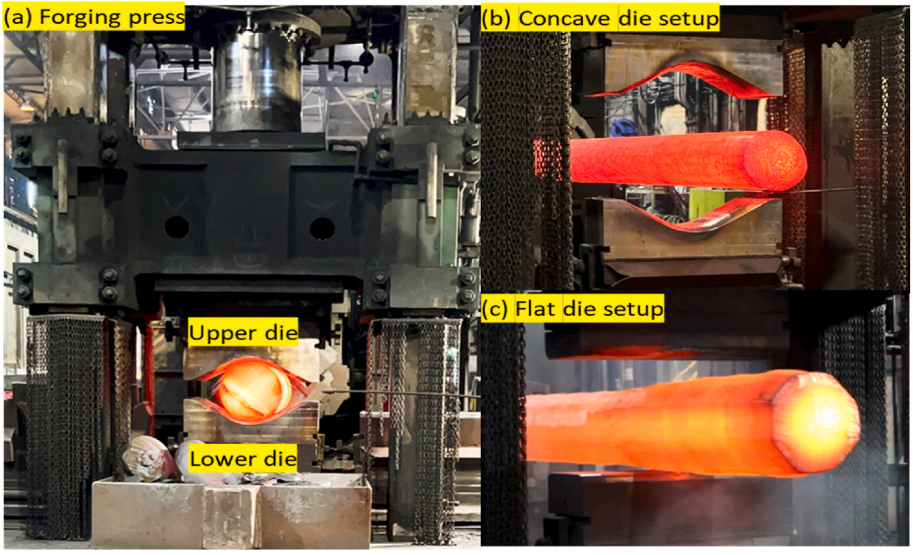

Fig. 11. Cogging setup at partner industry Finkl steel, Sorel, Canada (a) 2000 metric tons forging press (b) Concave and (c) Flat die setup.

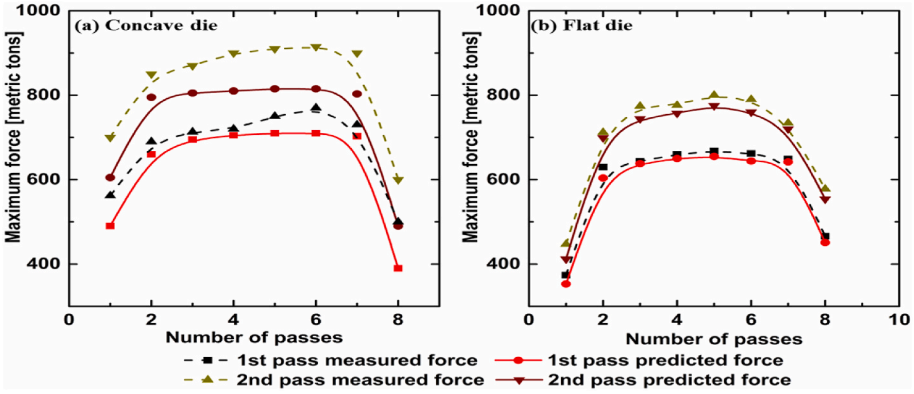

Fig. 12. Comparison of the measured and predicted maximum force for the initial 2 passes during the cogging process of an industrial size ingot of AISI H13 steel, as shown in (a) for the concave and (b) for the flat die.

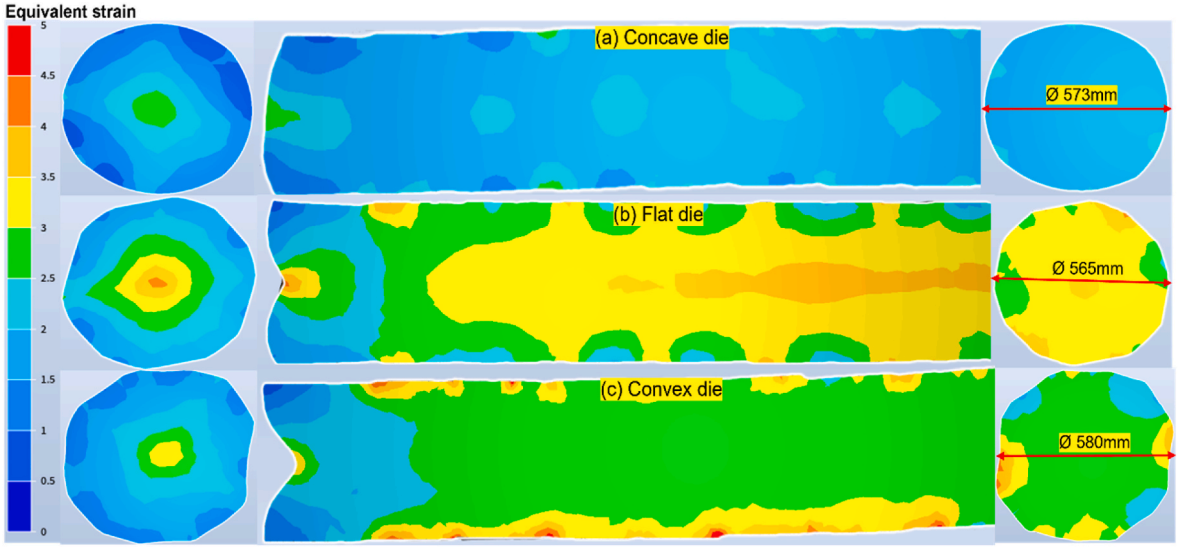

Fig. 13. The distribution of equivalent strain is shown along the longitudinal and transverse cross sections of the shaft after the cogging process using (a) concave, (b) flat, and (c) convex die.

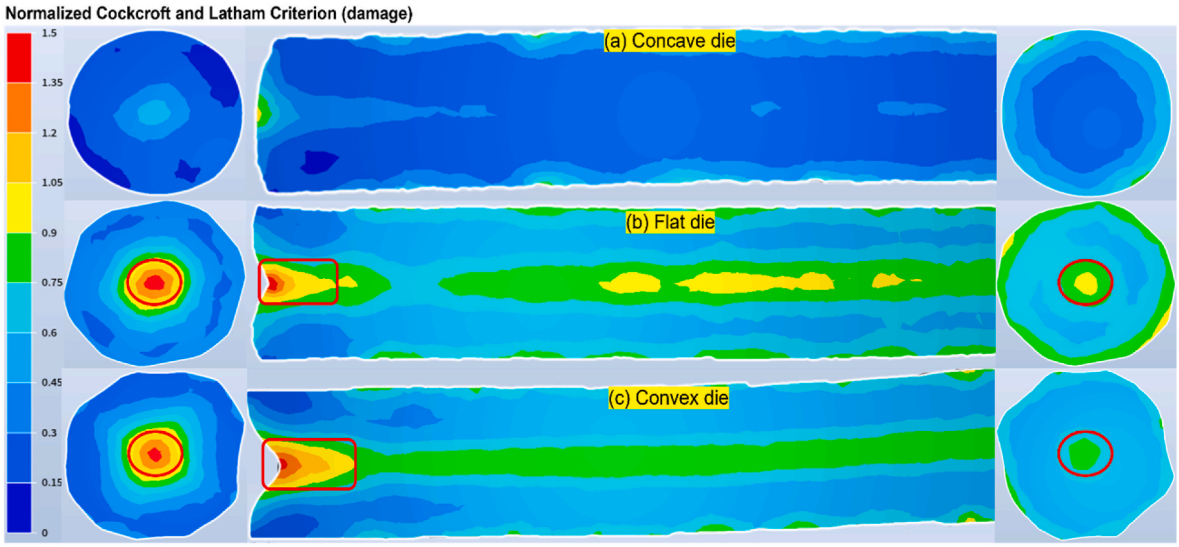

Fig. 14. Damage value distribution along longitudinal and transverse cross section of shaft at the end of cogging with (a) concave (b) flat and (c) convex die.

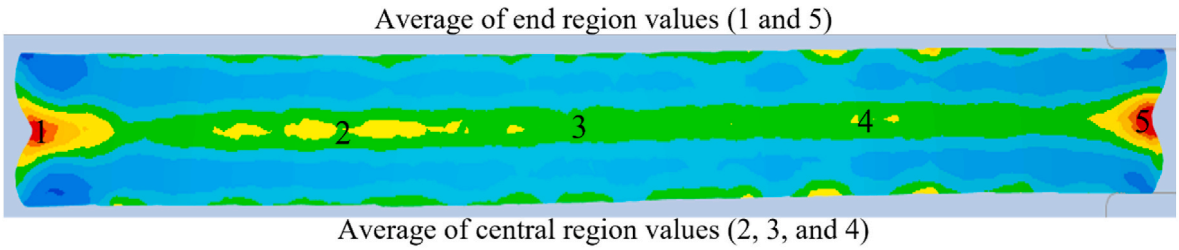

Fig. 15. Sensor location for data recording at the end of each pass.

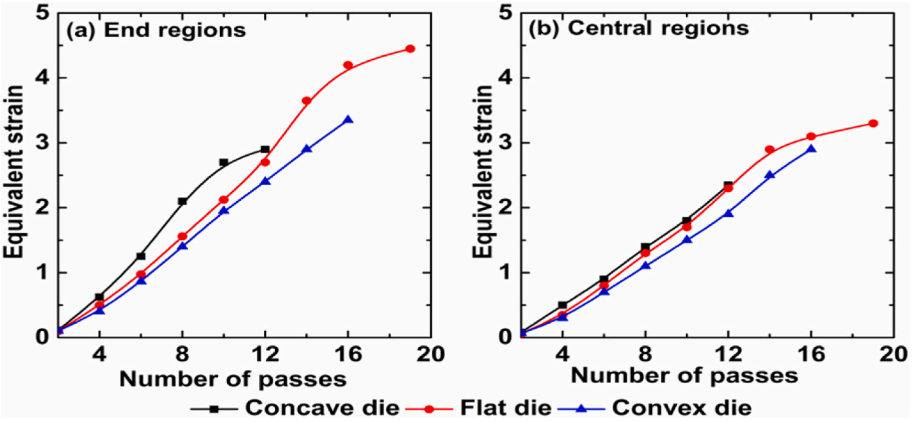

Fig. 16. Change in equivalent strain with the number of passes during the cogging of H13 steel, depicted as: (a) the average of two end values and (b) the average of values in the central region of the shaft.

average equivalent strain values at the end of cogging varied between 2.4 and 2.9 for the concave die, 3.3 and 4.5 for the flat die, and 2.9 and 3.4 for the convex die, encompassing both ends and the central region.

The results show that, employing the concave die led to higher equivalent strain values at both locations when compared to the flat and convex dies. Du [44] reported that during the forging of a railway axle, the equivalent strain at the workpiece center during forging with flat and concave anvils were 1.35 and 1.57, respectively. Xu et al. [45] in a similar study stated that the curvature of the concave die induced higher compressive deformation. Thus, by altering the die curvature, the deformation path and intensity of deformation were modified, leading to a more uniform deformation of the material.

5.1.2. *Damage value*

Based on the outcomes of the hot tensile tests, critical damage values were computed, revealing a variation ranging from 0.9 to 1 at temperatures of 800 °C and 1200 °C, respectively. Fig. 17 shows that with an increment in the number of passes, the damage value exhibited a linear rise both at the two ends and within the central region along the center axis of the shaft. The average damage values at the two ends were noted to be greater compared to the average value in the central region of the shaft. Initially, up to the 8th pass, the damage values for all die

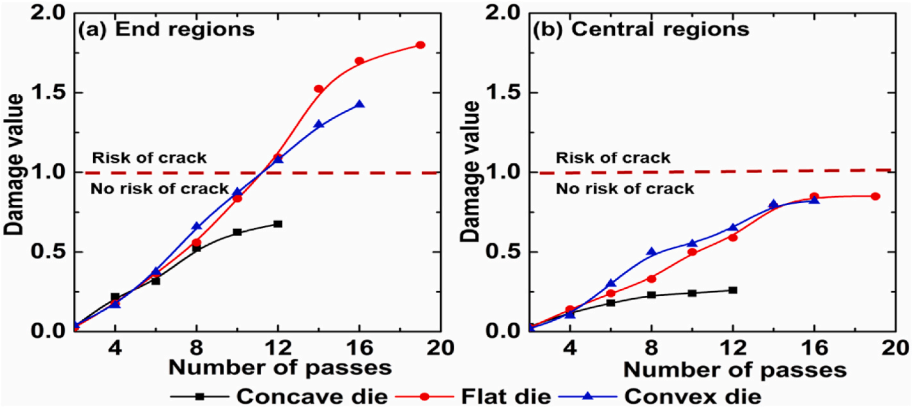

Fig. 17. Change in damage value with the increase in the number of passes during H13 steel cogging, shown as: (a) the average of two end values and (b) the average of values in the central region of the shaft.

geometries were quite similar. However, after the 8th pass, there was a swift increase to 1.5 and 1.8 for the flat and convex dies, respectively. In contrast, for the concave die, the damage value increased at a comparatively slower rate, reaching 0.7 at the end of the cogging. Hence, minimizing the number of passes to attain the desired shaft dimensions is of utmost significance. This investigation revealed that utilizing the concave die allowed reaching the required final dimensions in as few as 12 passes, compared to 19 passes with the flat die and 16 passes with the convex die.

5.1.3. Maximum shear stress

The critical threshold for the maximum shear stress was determined as 62.5 MPa through the hot tensile tests. Fig. 18 demonstrates the change in the maximum shear stress as the number of passes increases during the cogging process. The findings indicate a linear increase in the maximum shear stress value as the number of passes is increasing, both at the two ends and within the central region along the center axis of the shaft. The average maximum shear stress values at the two ends were noted to be higher than the average values in the central region. At the end of cogging, the average maximum shear stress in the central region and at the two ends of the shaft ranged from 26 to 60 MPa for the concave die, 36–84 MPa for the flat die, and 29–66 MPa for the convex die. Fig. 18(a) shows the average value of the maximum shear stress at the end of the cogging for the two ends of the shaft for flat and convex dies. Notably, this value surpasses the critical threshold for crack initiation, indicating a definite potential for center burst and crack formation. Fig. 18(b) shows the average values within the central region of the shaft for the three die geometries. These values remain below the critical stress threshold (62.2 MPa), implying a minimal risk of crack occurrence. Using the concave die geometry, the maximum shear stress value was below the critical threshold in all regions, in contrast to the flat and convex dies. Therefore, with concave die curvature, it was possible to reduce the maximum shear stress value to approximately 60 MPa.

5.1.4. Stress triaxiality

The critical stress triaxiality value, necessary to prevent the initiation and formation of cracks in the material, should be equal to or lower than dotted line in Fig. 19 (−0.3) [46]. A high negative value reduces the risk of central burst formation [47]. Fig. 19 shows the variation of stress triaxiality with the number of passes during cogging. Unlike equivalent strain, damage value and maximum shear stress value, the stress triaxiality value in the central region demonstrates a decrease (more negative value) with the rising number of passes, in contrast to the average value at the two ends of the shaft. Throughout the cogging process, the stress triaxiality variation curve exhibited a sinusoidal waveform. This phenomenon arises from the alternating compressive and tensile stress states that the material undergoes along the center axis of the shaft with each pass; as the number of passes increases, and as the average stress triaxiality in the central region decreases.

The average stress triaxiality values at the extreme ends for all three dies are illustrated in Fig. 19(a). The results show that the stress triaxiality values for the concave die range between −0.2 and −0.7, with the majority of values situated in the region of no crack risk. Similar results were obtained for the central region, as presented in Fig. 19(b). It can be seen that the smallest triaxiality stress values are for the concave die; although, in this case, the two other dies also fall within the safe zone; however, the values are still significantly higher than the ones for the

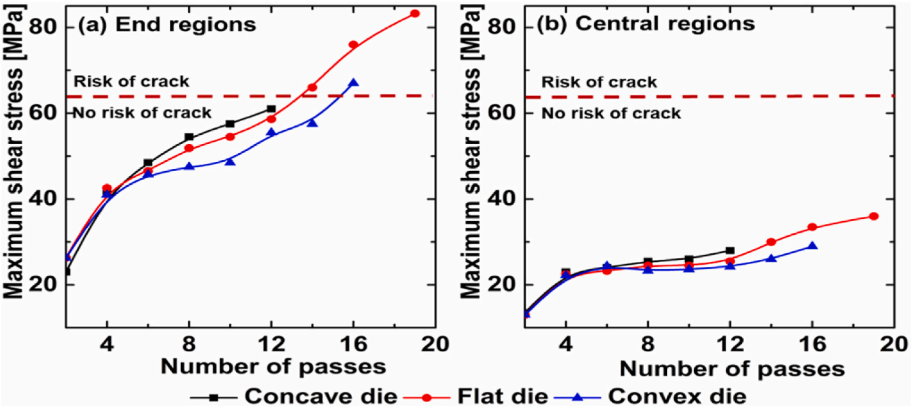

Fig. 18. Change in maximum shear stress with the increase in the number of passes during the cogging of H13 steel, depicted as: (a) the average of two end values and (b) the average values in the central region of the shaft.

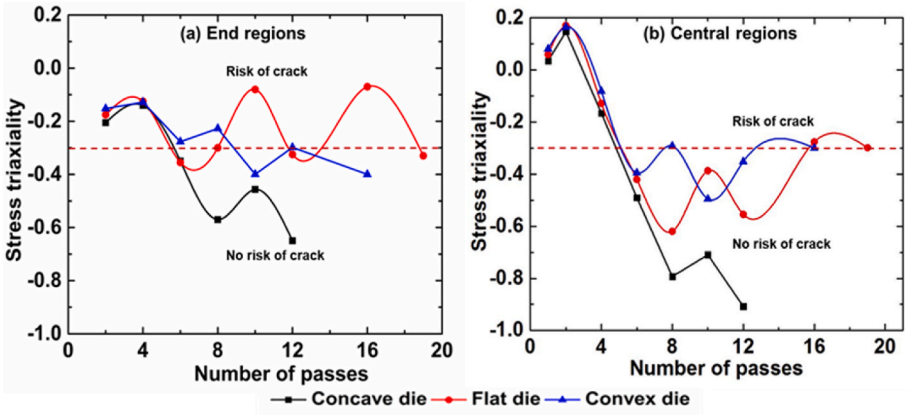

Fig. 19. Variation of stress triaxiality with the increase in the number of passes during the cogging of H13 steel, represented as: (a) the average of two end values and (b) the average values in the central region of the shaft.

concave die. The large negative value indicates the presence of dominant compressive deformation and stress states along the center axis of the workpiece.

A comparison between the three die geometries that summarizes the above results is provided in Table 7, all the parameter values were reported from the extreme end to the central region at the end of cogging. Where it can be seen that the concave die configuration yields to more uniform deformation distribution, maximum shear stress, and lower damage values featuring a notably negative stress triaxiality value of −0.9 (indicative of compressive stress states), in contrast to the flat die. Furthermore, the comparison demonstrates that all the parameter values for the convex die fall within the range between concave and flat dies.

The above results are in agreement with those of Yang et al. [10] who emphasized the significance of maximum shear stress and maximum tensile stress (first principal stress) as crucial factors influencing the formation and propagation of center burst formation. The results reported by Zhou et al. [13]on the role of tensile and maximum shear stresses on central crack formation during cross wedge rolling are confirmed by our study for cogging of AISI H13. Specifically, our analysis showed that the maximum shear stress initiated void formation, while principal stress expedited crack propagation. Kukuryk [17] study involved the examination and comparison of three ductile damage criteria. The analysis also revealed that the normalized Cockcroft and Latham damage criterion was an efficient measure for ductile damage prediction during the cogging process.

Fig. 16 shows that equivalent strain variation with the same amount of deformation per blow, the concave die induces a greater level of compressive deformation at the center of the shaft than the flat and convex dies. This observation might be attributed to the larger contact area achieved with the concave die in contrast to the other two die geometries. The increased contact area with the workpiece surface, coupled with the inward shape of the die, results in greater constraining of the lateral material flow [48]. For flat and convex dies, the contact area was smaller, and there was less control over the lateral material flow. The obtained results are in agreement with those of [17] who studied the effect of the convex anvils on the stress state and fracture prediction in two stage cogging of a stainless steel bar.

Figs. 17 and 18 show that the accumulation of damage and maximum shear stress value primarily occurs along the center axis of the shaft, with the highest values concentrated at the two ends of the shaft. This pattern amplifies the risk of crack initiation. Cogging using flat or convex dies surpasses the upper limit of the critical damage value (i.e., 1) and the maximum shear stress value of 62.5 MPa at the end of the cogging process. In such circumstances, the material becomes susceptible to cracking. Fig. 19 presents the stress triaxiality variation in relation to the number of passes. It must be noted that cogging with flat or convex dies resulted in slightly negative stress triaxiality values (ranging from −0.1 to −0.3 at the two ends of the shaft). In contrast, the use of the concave die yielded stress triaxiality values ranging between −0.2 and −0.7 at the end of cogging. Therefore, the concave die generates more pronounced compressive stresses and deformation at the center, accompanied by smaller damage values (0.3–0.7) and uniform deformation. Therefore, concave die curvature provides more compressive stress-strain states compared to flat and convex die.

Table 7
Comparison and summary of above results.

Parameters	Concave die	Flat die	Convex die
Number of passes requires to achieve final diameter (571 mm)	12	19	16
Equivalent strain	2.4 to 2.9	3.3 to 4.5	2.9 to 3.4
Damage value	0.3 to 0.7	0.8 to 1.8	0.8 to 1.4
Maximum shear stress (MPa)	28 to 60	36 to 84	29 to 66
Stress triaxiality	−0.7 to −0.9	−0.32 to −0.3	−0.4 to −0.3

5.1.5. *Heterogeneity in equivalent strain distribution*

Study of heterogeneous distribution of equivalent strain holds importance for the forging process. In case of bulk forming process, inhomogeneities in distribution of plastic strain impact the deformation behavior, microstructure and mechanical properties [49,50]. The heterogeneity index was calculated by measuring the equivalent strain in each of the 126121 elements, in the entire forged bar at the end of 12 passes. In this study, the coefficient of variation (CoV) is introduced as a heterogeneity index for cogging process studies. The coefficient of variation is computed by dividing the standard deviation by the mean value [51]. In the recent studies available in the literature, heterogeneity in the ring rolling process was expressed using the CoV [52]. The dimensionless value CoV, offers insight into the level of variability in relation to the mean within a population. A larger value of CoV indicates a higher level of non-uniformity in distribution. The mean (μ) and standard deviation (σ) were computed using the formulae provided in Eq. (16) and Eq. (17) respectively. Eq. (18) is employed to determine the coefficient of variation, as demonstrated below.

$$\mu = \Sigma_{i=1}^{N} \bar{\varepsilon}_i / N \tag{16}$$

$$\sigma = \sqrt{\frac{\Sigma_{i=1}^{N} (\bar{\varepsilon}_i - \mu)^2}{N-1}} \tag{17}$$

$$CoV = \frac{\sigma}{\mu} \tag{18}$$

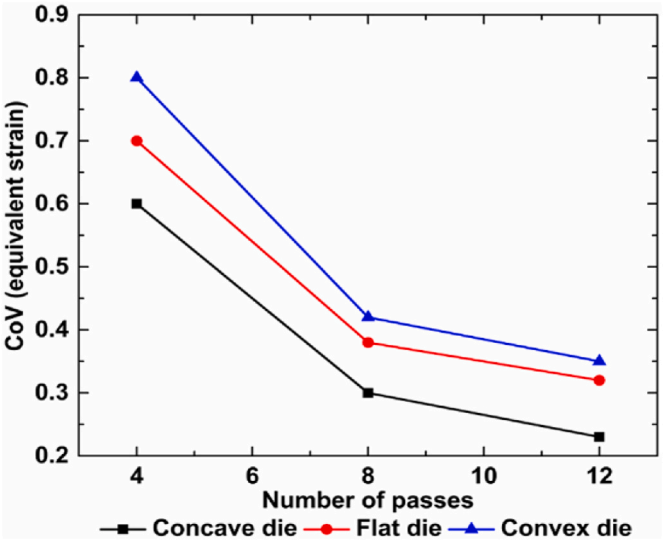

Fig. 20. Shows the CoV variation of equivalent strain with an increase number of passes.

Where, N is the number of elements in the entire ingot. $\bar{\varepsilon}_i$ equivalent strain corresponding to a single element.

Fig. 20 shows the variation of CoV as a function of the number of passes during the cogging process with concave, flat and convex die. It is observed that as the number of passes increases, the CoV value decreases which results in better homogeneity in strain distribution. This indicates decrease in heterogeneity in equivalent strain distribution as the number of passes increases. Cogging with concave die provides more uniform deformation compared to the flat and convex die. Figs. 16 and 20 show that cogging process with concave die helps in obtaining higher strain levels and uniform deformation compared to flat and convex die and staying below the cracking threshold.

The new approach of using concave die during the cogging of AISI H13 steel has been implemented in the industry as shown in Fig. 11(c). Resulting in the elimination of the center burst defects while the number of passes were reduced from 19 to 12; thereby, reducing energy consumption and increasing the production output.

6. Conclusions

This study comprises of development of constitutive model for AISI H13 steel. This model was then implemented via user subroutine to develop a 3D thermo-mechanically coupled FE model of industrial cogging process. The developed FE model was validated using industrial data. The cogging process was optimized using a series of FE simulations run to ascertain the effect of the deformation path defined by die geometry (concave, flat and convex) on the stress-strain states and damage evolution along the central axis of the shaft. The objective was to anticipate critical regions prone to center burst formation during the cogging of AISI H13 steel. Complete information on risky zone for the center burst formation was obtained and the best die geometry for the cogging process has been identified. The key findings and conclusions drawn from this study could be summarized as.

1. An optimum material model was developed based on the Arrhenius constitutive model and validated with experimental flow stress data. It shows more accurate prediction compared to the Hansel - Spittel and Johnson - Cook model. Additionally, the critical damage value for the forging temperature range was determined.
2. The developed material and damage model were integrated into the Forge NxT 3.2® and cogging process was simulated for industrial size ingot. The validated FE model offers the capability to forecast the risky area prone to center burst formation during cogging.
3. The concave die provided more uniform and higher compressive deformation, along with lower damage values compared to the flat and convex die during the cogging of highly sensitive material AISI H13 steel.
4. A novel approach and application of concave die in cogging were implemented in the industry and resulted in an elimination of center burst in the shaft and increased production output.

Credit author statement

Prashant Dhondapure: Conceptualization, Methodology, Visualization, Formal analysis, Validation, Writing – original draft. Pierre Tize Mha: Methodology, Writing – review & editing. Soumyaranjan Nayak: Methodology, Data curation, Writing – review & editing. Lea Ebacher: Data curation, Investigation. Simin Dourandish: Methodology, Resources. Henri Champliaud: Supervision, Writing – review & editing. Jean-Benoit Morin: Resources, Writing – review & editing. Mohammad Jahazi: Supervision, Conceptualization, Resources, Writing – review & editing, Project administration, Funding acquisition.

Declaration of competing interest

The authors declare that they have no known competing financial interests or personal relationships that could have appeared to influence the work reported in this paper.

Acknowledgments

This work was funded by Finkl Steel-Sorel and MITACS through a grant number [IT164670]. We would like to thanks Mr. Radu Romanica for conducting the Gleeble experiment precisely. We also appreciate help and support Mr. Patrice Lasne and Mr. John Swanson from Transvalor for helping us to implement a new material model into the Forge NxT® 3.2 software.

References

[1] Li B, Zhang S, Zhang Q, Chen J, Zhang J. Modelling of phase transformations induced by thermo-mechanical loads considering stress-strain effects in hard milling of AISI H13 steel. Int J Mech Sci 2018;149:241–53. https://doi.org/10.1016/j.ijmecsci.2018.10.010.
[2] Marashi J, Yakushina E, Xirouchakis P, Zante R, Foster J. An evaluation of H13 tool steel deformation in hot forging conditions. J Mater Process Technol 2017;246:276–84. https://doi.org/10.1016/j.jmatprotec.2017.03.026.
[3] Dourandish S, Champliaud H, Morin JB, Jahazi M. Microstructure-based finite element modeling of a martensitic stainless steel during hot forging. Int J Adv Manuf Technol 2022;123:2833–51. https://doi.org/10.1007/s00170-022-10306-z.
[4] Bulzak T, Pater Z, Tomczak J, Majerski K. Hot and warm cross-wedge rolling of ball pins - comparative analysis. J Manuf Process 2020;50:90–101. https://doi.org/10.1016/j.jmapro.2019.12.001.
[5] Zhenwei W, Jianping W, Changwen H, Jiabing S, Baoguo X, Xingquan Z. Cracking failure analysis of steel piston forging die. Eng Fail Anal 2022;138:106291. https://doi.org/10.1016/j.engfailanal.2022.106291.
[6] Krishna BV, Sidhu RK. Analysis of center burst during hot forging. J Fail Anal Prev 2002;2:61–6. https://doi.org/10.1007/bf02715471.
[7] Genel K. Boriding kinetics of H13 steel. Vacuum 2006;80:451–7. https://doi.org/10.1016/j.vacuum.2005.07.013.
[8] Mahlami CS, Pan X. Mechanical properties and microstructure evaluation of high manganese steel alloyed with vanadium. AIP Conf Proc 2017;1859. https://doi.org/10.1063/1.4990236.
[9] Yuan L, Wei Q, Han L, Shan D, Guo B. A new hot forging method for the die temperature higher than the billet temperature. Int J Adv Manuf Technol 2021;116:3063–74. https://doi.org/10.1007/s00170-021-07656-5.
[10] Yang C, Dong H, Hu Z. Micro-mechanism of central damage formation during cross wedge rolling. J Mater Process Technol 2018;252:322–32. https://doi.org/10.1016/j.jmatprotec.2017.09.041.
[11] Lee HW, Lee GA, Yoon DJ, Choi S, Na KH, Hwang MY. Optimization of design parameters using a response surface method in a cold cross-wedge rolling. J Mater Process Technol 2008;201:112–7. https://doi.org/10.1016/j.jmatprotec.2007.11.287.

[12] Zhou X, Shao Z, Pruncu CI, Hua L, Balint D, Lin J, et al. A study on central crack formation in cross wedge rolling. J Mater Process Technol 2020;279. https://doi.org/10.1016/j.jmatprotec.2019.116549.
[13] Zhou X, Shao Z, Zhang C, Sun F, Zhou W, Hua L, et al. The study of central cracking mechanism and criterion in cross wedge rolling. Int J Mach Tool Manufact 2020;159. https://doi.org/10.1016/j.ijmachtools.2020.103647.
[14] Zhou X, Sun C, Wang B, Jiang J. Investigation and prediction of central cracking in cross wedge rolling. Int J Adv Manuf Technol 2022;123:145–59. https://doi.org/10.1007/s00170-022-10126-1.
[15] Li Q, Lovell MR, Slaughter W, Tagavi K. Investigation of the morphology of internal defects in cross wedge rolling. J Mater Process Technol 2002;125–126:248–57. https://doi.org/10.1016/S0924-0136(02)00303-5.
[16] Kukuryk M. Experimental and FEM analysis of void closure in the hot cogging process of tool steel. Metals 2019;9(5):538. https://doi.org/10.3390/met9050538.
[17] Kukuryk M. Analysis of deformation, the stressed state and fracture predictions for cogging shafts with convex anvils. Materials 2021;14. https://doi.org/10.3390/ma14113113.
[18] Han Y, Li C, Ren J, Qiu C, Li E, Chen S. Characterization of hot deformation behavior and processing map of as-Cast H13 hot work die steel. Met Mater Int 2021;27:3574–89. https://doi.org/10.1007/s12540-020-00863-x.
[19] Chen S, Qin Y, Chen JG, Choy CM. A forging method for reducing process steps in the forming of automotive fasteners. Int J Mech Sci 2018;137:1–14. https://doi.org/10.1016/j.ijmecsci.2017.12.045.
[20] Park J, Kim Y, Jeong H, Kwon H, Kwon Y, Kim N. Cogging process design of M50 bearing steel for billet quality. J Mater Res Technol 2023;26:5576–93. https://doi.org/10.1016/j.jmrt.2023.08.275.
[21] Connolly D, Sivaswamy G, Rahimi S, Vorontsov V. Miniaturised experimental simulation of open-die forging. J Mater Res Technol 2023;26:3146–61. https://doi.org/10.1016/j.jmrt.2023.08.073.
[22] Markov OE, Perig AV, Zlygoriev VN, Markova MA, Grin AG. A new process for forging shafts with convex dies. Research into the stressed state. Int J Adv Manuf Technol 2017;90:801–18. https://doi.org/10.1007/s00170-016-9378-6.
[23] Dudra SP, Im YT. Analysis of void closure in open-die forging. Int J Mach Tool Manufact 1990;30:65–75. https://doi.org/10.1016/0890-6955(90)90042-H.
[24] Zhang X, Ma F, Ma K, Li X. Multi-scale analysis of void closure for heavy ingot hot forging. Mod Appl Sci 2012;6:15–25. https://doi.org/10.5539/mas.v6n10p15.
[25] Tamura K, Tajima J. Optimisation of open die forging condition and tool design for ensuring both internal quality and dimensional precision by three-dimensional rigid-plastic finite element analysis. Ironmak Steelmak 2003;30:405–11. https://doi.org/10.1179/030192303225001801.
[26] Kukuryk M. Analysis of deformation and prediction of cracks in the cogging process for die steel at elevated temperatures. Materials 2020;13:1–17. https://doi.org/10.3390/ma13245589.
[27] Ghiotti A, Fanini S, Bruschi S, Bariani PF. Modelling of the Mannesmann effect. CIRP Ann - Manuf Technol 2009;58:255–8. https://doi.org/10.1016/j.cirp.2009.03.099.
[28] Lin L, Wang B, Zhou J, Shen J. Manufacturing large shafts by a novel flexible skew rolling process. Int J Adv Manuf Technol 2022;118:2833–51. https://doi.org/10.1007/s00170-021-08079-y.
[29] ASTM E8 standard test methods for tension testing of metallic materials 1. Annual Book of ASTM Standards 4 2010:1–27. https://doi.org/10.1520/E0008.
[30] Sellars CM, McTegart WJ. On the mechanism of hot deformation. Acta Metall 1966;14(9):1136–8. https://doi.org/10.1016/0001-6160(66)90207-0.
[31] Jeong HY, Park J, Kim Y, Shin SY, Kim N. Processing parameters optimization in hot forging of AISI 4340 steel using instability map and reinforcement learning. J Mater Res Technol 2023;23:1995–2009. https://doi.org/10.1016/j.jmrt.2023.01.106.
[32] Nayak S, Dhondapure P, Singh AK, Prasad MJNV, Narasimhan K. Assessment of constitutive models to predict high temperature flow behaviour of Ti-6Al-4V preform. Advances in Materials and Processing Technologies 2020;6:296–310. https://doi.org/10.1080/2374068X.2020.1731233.
[33] Yin L, Wu Y. Comparison of constitutive models and microstructure evolution of GW103K Magnesium alloy during hot deformation. Materials 2022;15. https://doi.org/10.3390/ma15124116.
[34] Nalawade RS, Puranik AJ, Balachandran G, Mahadik KN, Balasubramanian V. Simulation of hot rolling deformation at intermediate passes and its industrial validity. Int J Mech Sci 2013;77:8–16. https://doi.org/10.1016/j.ijmecsci.2013.09.017.
[35] Johnson GR, Cook WH. Fracture characteristics of three metals subjected to various strains, strain rates, temperatures and pressures. Eng Fract Mech 1985;21:31–48. https://doi.org/10.1016/0013-7944(85)90052-9.
[36] Mha PT, Dhondapure P, Jahazi M, Tongne A. Interpolation and extrapolation performance measurement of analytical and ANN-based flow laws for hot deformation behavior of Medium Carbon steel. Metals 2023;13:663. https://doi.org/10.3390/met13030633.
[37] Niu L, Zhang Q, Wang B, Han B, Li H, Mei T. A modified Hansel-Spittel constitutive equation of Ti-6Al-4V during cogging process. J Alloys Compd 2022;894:162387. https://doi.org/10.1016/j.jallcom.2021.162387.
[38] Pasco J, McCarthy T, Parlee J, Nazri NA, Padmajan S, Rodrigues S, et al. Constitutive modeling of modified-H13 steel. MRS Communications 2022;12:343–51. https://doi.org/10.1557/s43579-022-00182-9.
[39] Oh SI, Chen CC, Kobayashi S. Ductile fracture in axisymmetric extrusion and drawing: Part 2 workability in extrusion and drawing. Journal of Manufacturing Science and Engineering, Transactions of the ASME 1979;101:36–44. https://doi.org/10.1115/1.3439471.
[40] Yang X, Zhang Z, Meng M, Jia J, Zhang H, Lei G, et al. Hot tensile deformation behaviors and a fracture damage model of the Mg-Gd-Y-Zn-Zr alloy. J Mater Res Technol 2022;18:255–67. https://doi.org/10.1016/j.jmrt.2022.02.104.
[41] Gontarz A, Piesiak J. Determining the normalized Cockroft-latham criterion for titanium alloy Ti6Al4V in tensile testing at room temperature. Proceedings of the World Congress on Mechanical, Chemical, and Material Engineering 2015;4–7.
[42] Stefanik A, Dyja H, Mróz S. Determination of the critical value of normalized Cocroft - Latham criterion during multi slight rolling based on tensile test. Arch Metall Mater 2011;56:543–50. https://doi.org/10.2478/v10172-011-0058-0.
[43] Cm G. Ductility and workability of metals. J of Metals 1968;96:2444.
[44] Du S, Li Y, Song J. Optimization of forging process parameters and anvil design for railway axle during high-speed forging. ASME International Mechanical Engineering Congress and Exposition 2015;1–6. https://doi.org/10.1115/IMECE2015-50695.
[45] Xu Y, Zhang Y, Zhuang X, Cao Z, Lu Y, Zhao Z. Numerical modeling and anvil design of high-speed forging process for railway axles. Int J Material Form 2021;14:813–32. https://doi.org/10.1007/s12289-020-01590-9.
[46] Geisler A, Sadeghifar M, Morin JB, Loucif A, Jahazi M. Void closure during open die forging of large size martensitic stainless-steel ingots: an experimental-analytical-numerical study. Int J Material Form 2023;16:1–11. https://doi.org/10.1007/s12289-022-01735-y.
[47] Bao Y, Wierzbicki T. On the cut-off value of negative triaxiality for fracture. Eng Fract Mech 2005;72:1049–69. https://doi.org/10.1016/j.engfracmech.2004.07.011.
[48] Dyja H, Banaszek G, Mróz S, Berski S. Modelling of shape anvils in free hot forging of long products. J Mater Process Technol 2004;157(158):131–7. https://doi.org/10.1016/j.jmatprotec.2004.09.022.
[49] Li B, Zhang S, Hu R, Zhang X. Dislocation density and grain size evolution in hard machining of H13 steel: numerical and experimental investigation. J Mater Res Technol 2020;9:4241–54. https://doi.org/10.1016/j.jmrt.2020.02.051.
[50] Nayak S, Singh AK, Prasad MJNV, Narasimhan K. Development of microstructural heterogeneities and dynamic restoration activity during ring rolling of Ti-6Al-4V alloy and its tensile response. J Alloys Compd 2023;963:171241. https://doi.org/10.1016/j.jallcom.2023.171241.
[51] Zhu S, Yang H, Guo LG, Gu RJ. Investigation of deformation degree and initial forming temperature dependences of microstructure in hot ring rolling of TA15 titanium alloy by multi-scale simulations. Comput Mater Sci 2012;65:221–9. https://doi.org/10.1016/j.commatsci.2012.07.014.
[52] Nayak S, Kumar Singh A, Gokhale H, Prasad MJNV, Narasimhan K. Optimization of Ti-6Al-4V ring rolling process by FE simulation using RSM. Int J Solid Struct 2023:262–3. https://doi.org/10.1016/j.ijsolstr.2022.112064. 112064.